Sustainable
Energy & Fuels

Spontaneous Mesostructure Formation Produces Optically Transmissive Ni-P Films That are Catalytically Active for the Photoelectrochemical Hydrogen Evolution Reaction

SCHOLARONE™
Manuscripts

Spontaneous Mesostructure Formation Produces Optically Transmissive Ni-P Films That are Catalytically Active for the Photoelectrochemical Hydrogen Evolution Reaction

Zachary P. Ifkovits,[1] Jillian T. Reed, [1] Paul A. Kempler,[1] Madeline C. Meier,[1] Sean T. Byrne,[1] Shaoyang Lin,[1] Alexandre Z. Ye,[1] Azhar I. Carim,[1,2] and Nathan S. Lewis[1,2]*

[1]Division of Chemistry and Chemical Engineering, California Institute of Technology, Pasadena, California 91125, USA.

[2]Beckman Institute Molecular Materials Resource Center, California Institute of Technology, Pasadena, California 91125, USA.

*Corresponding author: nslewis@caltech.edu

Abstract

Ni-P films that are catalytically active for the hydrogen-evolution reaction were electrodeposited onto photoactive Si substrates between 20 °C and 80 °C from an aqueous solution. Ni-P films deposited at 20 °C and exposed to acidic environments spontaneously developed deep cracks and a substantial increase in optical transmission to the semiconducting substrate resulted without affecting the catalytic performance of the film. In contrast, Ni-P films deposited at 80 °C only developed minor surface-level cracks and did not exhibit a substantial increase in optical transmission. During electrodeposition of the Ni-P films at low temperatures, the uptake of parasitically evolved hydrogen generated partially defective Ni-P, causing crack formation. Increases in the temperature of the electrodeposition bath increased the faradaic efficiency of Ni-P deposition and consequently reduced the uptake of parasitically generated hydrogen. The defective Ni-P films were converted to a crack-resistant material by thermally desorbing the excess hydrogen that was absorbed during the low-temperature electrodeposition process.

Introduction

Photoelectrochemical (PEC) water splitting often requires coating semiconducting light absorbers with metal or metal-oxide electrocatalysts to drive the hydrogen- and oxygen-evolution reactions, respectively.[1] Typically, the integration of catalysts with light absorbers entails optimization of an inherent trade-off between catalytic activity and optical transmissivity. Increasing the mass-loading of the catalyst generally increases the catalytic activity of the photoelectrode per unit of projected electrode area, but blocks additional light from reaching the semiconductor substrate under front-face illumination.[2]

Approaches to control the macro- and micro-structure of catalysts to obtain increased optical transmissivity include lithographic, 3D electrode fabrication, and device design processes. Lithographic techniques and control over the thickness of the catalyst layer have been utilized to coat films of catalytic materials on semiconductor surfaces.[3-4] Microstructuring of semiconductor substrates into microwires, cones, or other morphologies, followed by selective placement of electrocatalysts, has been utilized to obtain high loadings of Ni-Mo, Co-P, Pt, Cu, and others materials for PEC electrolysis or CO_2 reduction reactions, producing increases in energy-conversion efficiency when compared to planar electrode counterparts.[5-10] Controlled electrodeposition techniques have been used to pattern catalysts in discrete islands, allowing for light to pass between the particles.[11-12] Additionally, several template-free microstructuring approaches have been used to produce desirable microscale patterns over large areas.[13]

Electrodeposited Co-P films that initially are dense, metallic, and optically opaque develop cracks upon exposure to acidic environments, allowing for a substantial amount of incident illumination to reach the semiconductor substrate.[14] This structuring occurs spontaneously and does not require external patterning or structure-directing agents. We report herein the implementation of this approach for another electrocatalytic film, Ni-P, that also allows use of earth-abundant elements, as opposed to platinum group metals, to catalyze the hydrogen-evolution reaction while allowing for high optical transmission to an underlying photocathode for use in PEC-based solar fuel production.

Ni-P electrocatalysts have been studied extensively for use as hydrogen evolution catalysts and have been thoroughly characterized on electrode surfaces using x-ray photoelectron spectroscopy (XPS), x-ray diffraction (XRD), transmission- and scanning electron microscopy (TEM/SEM), among other methods.[15-17] Ni-P is a promising candidate for this analysis due to its

low (~50 – 200 mV) overpotential at -10 mA cm^{-2}, low (30-90 mV dec.$^{-1}$) Tafel slope, near-unity faradaic efficiency towards hydrogen evolution, relative synthetic ease, and similarity to Co-P films that have been shown to spontaneously form optically transmissive layers.[14-15, 18]

Results and Discussion

Ni-P films were grown by cathodic electrodeposition on Si electrodes that had been pre-seeded with ~2 nm of sputtered Ni on top of a thin sputtered layer of Ti. The deposition bath was an aqueous solution of 0.15 M H$_3$BO$_3$, 0.10 M NaCl, 0.30 M H$_2$NaPO$_2 \cdot$H$_2$O, and 0.20 M NiCl$_2$, with the pH adjusted to 3.5 using H$_3$PO$_2$. The temperature of the deposition bath was varied between 20 °C and 80 °C.
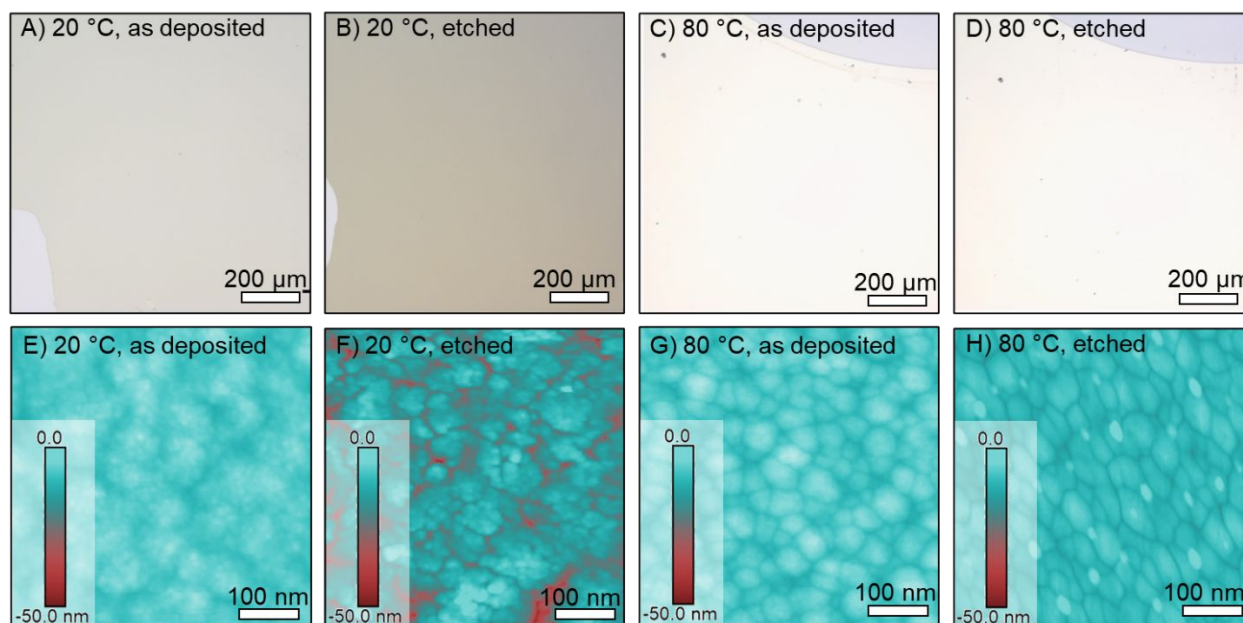
Figure 1. Color optical micrographs of electrodeposited Ni-P films at (a) 20 °C, (b) 20 °C, followed by a 60 s etch in 0.50 M H$_2$SO$_4$, (c) 80 °C, (d) 80 °C, after a 60 s etch in 0.50 M H$_2$SO$_4$. Grey areas are the Si substrate. Atomic force micrographs of electrodeposited Ni-P films at (e) 20 °C, (f) 20 °C followed by a 300 s etch in 0.50 M H$_2$SO$_4$, (g) 80 °C, (h) 80 °C followed by a 300 s etch in 0.5 M H$_2$SO$_4$.

Color optical micrographs and scanning electron micrographs (SEMs) of Ni-P films that were electrodeposited at a current density of -20 mA cm^{-2} for 20 s onto n$^+$-Si/Ti/Ni electrodes at 20 °C (NiP$_{20°C}$) showed smooth, reflective layers of Ni-P that were ~ 90 nm thick (Figure 1a, Figures S1-S3). During electrodeposition at 20 °C, bubbles formed on the electrode surface, indicative of H$_2$(g) evolution in addition to deposition of Ni-P (Figure S4a). Bubbles formed on the NiP$_{20°C}$ surface during subsequent immersion in 0.50 M H$_2$SO, and after immersion the NiP$_{20°C}$

films appeared darker visually (Figure 1b). In contrast, Ni-P films that were electrodeposited at 80 °C (NiP$_{80°C}$) were lighter in color than as-deposited NiP$_{20°C}$ films and were ~100 nm thick (Figure 1c, Figure S3). No bubbles were observed visually during electrodeposition at 80 °C (Figure S4b), indicating that the faradaic efficiency for Ni-P deposition increased as the temperature increased. Anodic stripping of the Ni-P films in a 1 mM H$_2$SO$_4$ solution indicated that the faradaic efficiency of Ni-P deposition was ~ 65% for NiP$_{20°C}$ and 95% for NiP$_{80°C}$ (Figure S5). This behavior is consistent with previous observations that the faradaic efficiency of Ni-P deposition increases as the temperature of the deposition bath increases.[19-20] The voltage required to maintain the deposition current density at -20 mA cm^{-2} was more positive (-0.65 V vs. the saturated calomel electrode, SCE) at 80 °C than at 20 °C (-0.92 V vs. SCE), consistent with the electrodeposition behavior of other nickel alloys.[21] NiP$_{80°C}$ films did not show a substantial color change as a result of immersion in 0.50 M H$_2$SO$_4$ (Figure 1d). Atomic force micrographs (AFMs) showed that immersion in 0.50 M H$_2$SO$_4$ resulted in cracks through the NiP$_{20°C}$ films (Figure 1e-f), whereas NiP$_{80°C}$ films showed no change in morphology due to immersion in 0.50 M H$_2$SO$_4$ (Figure 1g-h).

The change in the nanoscale morphology of NiP$_{20°C}$ films due to immersion in H$_2$SO$_4$ increased the amount of incident illumination that reached the semiconductor substrate. The resulting increased light absorption by the substrate resulted in the visual darkening of the overlying NiP$_{20°C}$ films. In contrast, NiP$_{80°C}$ films did not undergo substantial morphology changes, or display visual changes, due to immersion in 0.50 M H$_2$SO$_4$.

Energy-dispersive X-ray spectroscopy (EDX) indicated that the Ni-P films were Ni-rich, with an initial atomic Ni fraction of 92% and 89% for NiP$_{20°C}$ and NiP$_{80°C}$ films, respectively (Figure S6). Additional EDX of sample cross sections did not indicate a compositional gradient along the film depth (Table S1). X-ray photoelectron spectroscopy (XPS) of the P *2p* and Ni *2p* regions indicated the formation of Ni-P bonds and showed a decrease in surface Ni-O and P-O formation as the deposition temperature increased (Figure S7, Table S2). The formation of surface oxides is consistent with a more highly reactive, therefore more unstable Ni-P surface as the deposition temperature decreased. After immersion for 300 s in 0.50 M H$_2$SO$_4$, EDX indicated a decrease of the composition in the bulk of NiP$_{20°C}$ films to an atomic Ni fraction of 88%, whereas no substantial change was observed in the composition of NiP$_{80°C}$ films (Figure S6). This behavior is consistent with previous reports of preferential dissolution of Co from Co-P during exposure to acidic electrolytes.[6]

Cyclic voltammograms of $NiP_{20°C}$ films on photoactive n^+p-Si/Ti/Ni substrates showed an increase in the cathodic photocurrent density at 0 V vs. RHE (J_{ph}) due to electrochemical cycling in 0.50 M H_2SO_4 that was purged continuously with H_2(g) under simulated AM 1.5 illumination (Figure 2a, blue). Between voltammograms, samples were held at open circuit (~ 0 V vs the reversible hydrogen electrode, RHE) for 180 s in the absence of illumination. The $|J_{ph}|$ of $NiP_{20°C}$ increased from 5.3 mA cm^{-2} to 12.1 mA cm^{-2} over the activation period. The onset potential for cathodic current did not shift during the activation period, indicating no loss in catalytic activity. Over the same activation period, $|J_{ph}|$ of $NiP_{80°C}$ only increased from 4.2 to 4.5 mA cm^{-2} (Figure 2a, red). SEMs of $NiP_{20°C}$ showed crack formation during device operation, with a final void fraction of ~20% (Figure 2b), whereas no apparent cracks were observed for $NiP_{80°C}$ (Figure 2c). The onset potential of n^+p-Si/Ti/Ni coated with $NiP_{80°C}$ films was ~150 mV more negative than the onset potential of n^+p-Si/Ti/Ni coated with $NiP_{20°C}$.
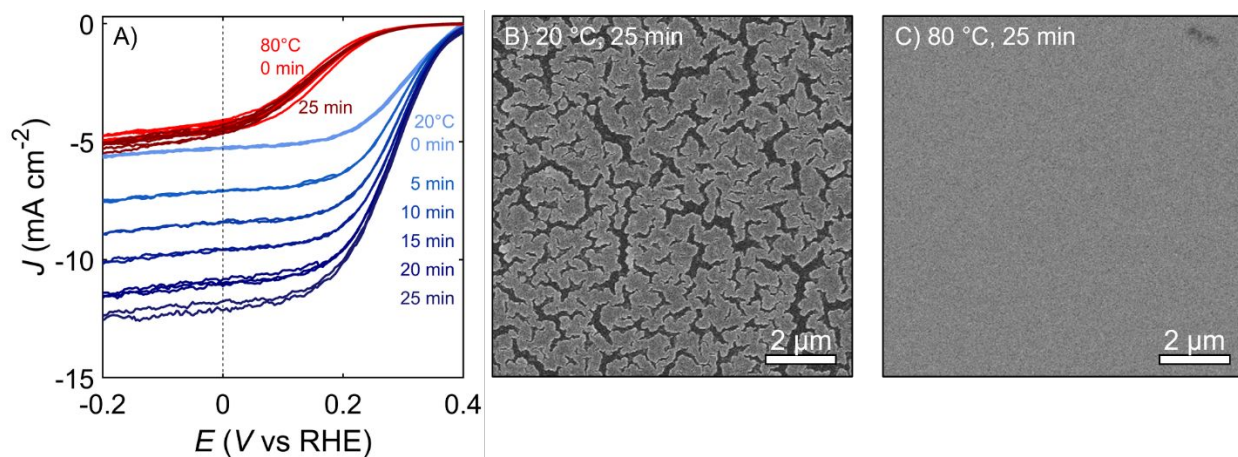
Figure 2. (a) Cyclic voltammograms of Ni-P films on n^+p-Si/Ti/Ni electrodes in 0.50 M H_2SO_4 purged continuously with H_2(g) under the equivalent of 100 mW cm^{-2} of solar Air Mass 1.5 illumination produced by a calibrated Xe lamp (b) Representative SEM of a sample deposited at 20 °C after photoelectrochemical experiments in 0.50 M H_2SO_4 (c) Representative SEM of a sample deposited at 80 °C after photoelectrochemical experiments in 0.50 M H_2SO_4.

The optical transmission (T_{opt}) of Ni-P films deposited onto a fluorine-doped SnO$_2$ (FTO) substrate increased as the etch time increased (Figures S8-S9). The average transmission ($T_{opt,avg}$) for as-deposited FTO/Ti/Ni/$NiP_{20°C}$ was 13% between 400 and 1100 nm. After immersion for 300 s in 0.50 M H_2SO_4, $T_{opt,avg}$ increased to 35%, and the void fraction of the film was ~8% (Figure S8-S10). Although the optical transmission should increase as the void fraction increases, an unetched Ni-P layer with an equivalent fractional coverage of 92% would transmit much less light

than the spontaneously nanostructured $NiP_{20°C}$ films. When the constituent components of a film are small relative to the wavelength of light, light is preferentially passed through the voids in the film due to a screening surface charge.[11] After 300 s of immersion in 0.50 M H_2SO_4 at open circuit, $T_{opt,avg}$ increased by 170%, 72%, 29%, and 37% for Ni-P films deposited at 20 °C, 40 °C, 60 °C, and 80 °C, respectively. No cracks deeper than 25 nm formed for $NiP_{60°C}$ or $NiP_{80°C}$ films, so the moderate increase in transmission is consistent instead with the formation of shallow < 20 nm cracks (Figure S11). $NiP_{80°C}$ films were less transmissive after immersion for 300 s ($T_{opt,avg\ 80°C,\ 300s}$ = 8.6%) in 0.50 M H_2SO_4 than the other films were before etching ($T_{opt,avg\ 20-60°C,\ 0\ s}$ = ~12%).

Spectroscopic ellipsometry on as-deposited $NiP_{20°C}$ films indicated that the extinction coefficient (k) was nearly constant at ~1.5, with a slight overall downward concavity vs wavelength (Figure 3a). Upon immersion in 0.50 M H_2SO_4, k decreased, which is consistent with an increase in optical transmission. In contrast, as-deposited $NiP_{80°C}$ exhibited a straight sloping increase in k from 2 to 4.3 as the wavelength increased. Moreover, the k of $NiP_{80°C}$ samples did not change substantially after exposure to 0.50 M H_2SO_4 and k of the $NiP_{80°C}$ film resembled that of a pure sputtered Ni film both before and after etching (Figure 3a). Upon heating an as-deposited $NiP_{20°C}$ film in air for 1 h at 250 °C h, k shifted from ~ 1.5 to yield a straight sloping increase from 1.5 to 3.3 as the wavelength increased. Furthermore, k did not change substantially upon exposure of the heated $NiP_{20°C}$ film to 0.50 M H_2SO_4 (Figure 3b). Both the shape of k and the similarity of k before and after exposure to 0.50 M H_2SO_4 indicate that the as-deposited $NiP_{20°C}$ film was converted by thermal treatment to a film that was optically similar to, and as chemically robust as, as-deposited $NiP_{80°C}$. Raw ellipsometric data of Ψ and Δ provided in the supporting information (Figure S12) likewise showed substantial optical changes for $NiP_{20°C}$ films upon etching in 0.50 M H_2SO_4, whereas the optical properties of $NiP_{80°C}$, Ni, and heated $NiP_{20°C}$ films did not change upon etching.

Gas chromatographs of the headspace of sealed vials that contained $NiP_{20°C}$, $NiP_{80°C}$, and bare Ni samples, respectively, showed that upon heating to 200 °C, $NiP_{20°C}$ samples released a substantially larger amount of $H_2(g)$ than $NiP_{80°C}$ samples, in a ratio of nearly 3:1 above the background (Figure 3c). The molar ratio of detected H to Ni in the films (H/Ni) was 0.09 and 0.02 for $NiP_{20°C}$ and $NiP_{80°C}$ films, respectively. Linear sweep voltammograms (LSVs) of as-deposited $NiP_{20°C}$ and $NiP_{80°C}$ films showed a substantial difference in the magnitude and position of the peak anodic current density in an unstirred solution of 1 mM H_2SO_4, 0.85 M $MgSO_4$, and 0.15 M $MgCl_2$ purged continuously with $N_2(g)$ (Figure 3d). The $NiP_{20°C}$ film showed a peak current

density of ~1.2 mA cm^{-2} at a potential of -0.26 V vs SCE, as well as a shoulder at more positive potentials. The NiP$_{80°C}$ film only showed a single feature of 0.5 mA cm^{-2} at -0.1 V vs. SCE. Previous studies of electrodeposited Ni films have shown that an anodic wave at ~ -0.2 V vs. SCE is indicative of a hydrogen-rich β-Ni phase, whereas an anodic wave at -0.1 V vs. SCE is indicative of a hydrogen-deficient α-Ni phase.[22-23] The integrated charge density in the stripping waves is shown in the supporting information (Figure S5).
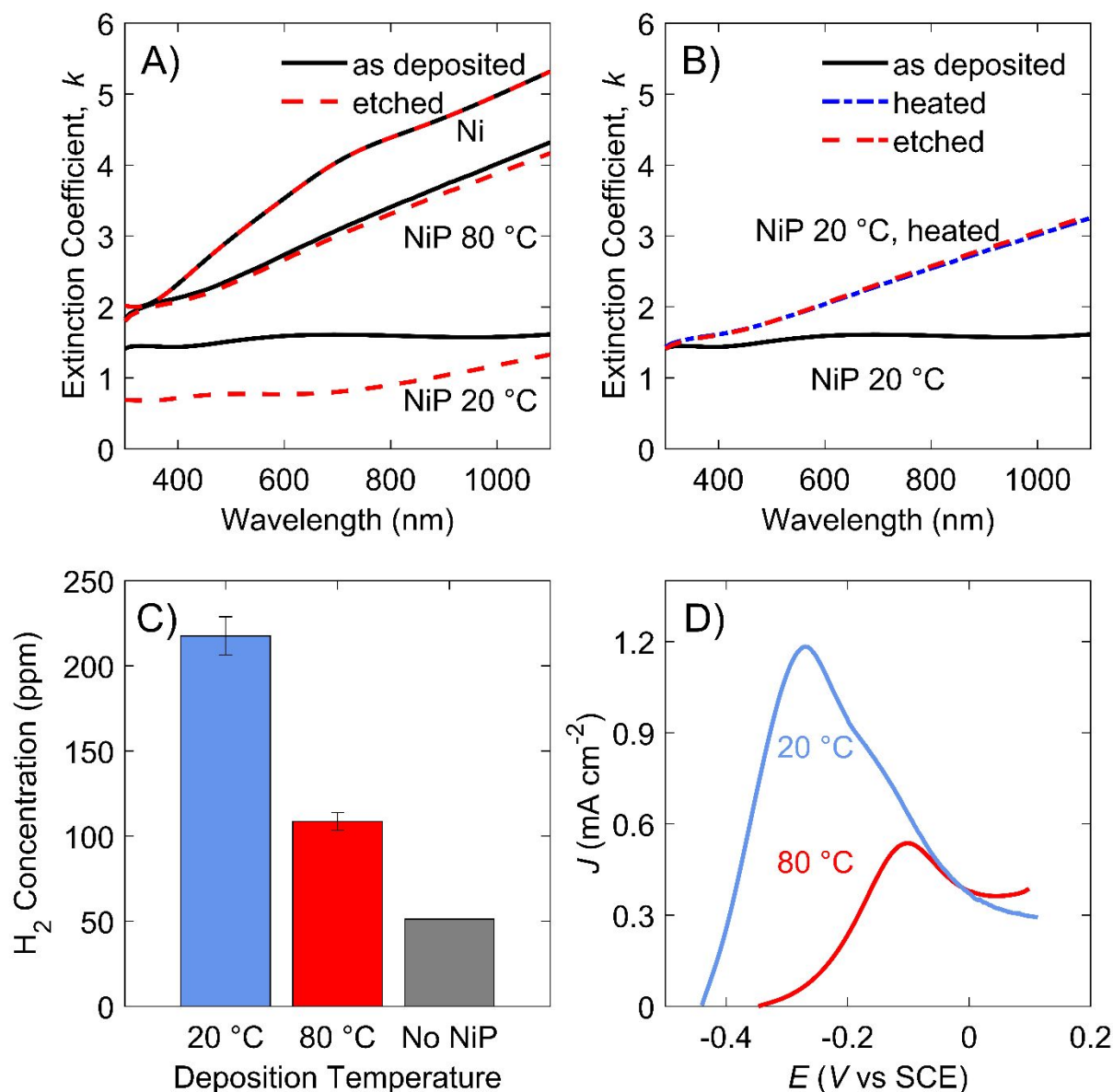
Figure 3. Extinction coefficient (*k*) of Ni-P films on Si substrates measured by spectroscopic ellipsometry for as deposited (black) and etched (red) samples of (a) NiP$_{20°C}$, NiP$_{80°C}$, sputtered Ni, and (b) NiP$_{20°C}$ heated

to 250 °C in air. (c) Headspace H_2 concentration of $NiP_{20°C}$ (blue), $NiP_{80°C}$ (red), and bare $n^+Si/Ti/Ni$ substrate (gray) samples after heating to 200 °C in a sealed vial. (d) LSVs of as-deposited $NiP_{20°C}$ and $NiP_{80°C}$ films in an unstirred solution of 1 mM H_2SO_4, 0.85 M $MgSO_4$, and 0.15 M $MgCl_2$ purged continuously with $N_2(g)$

Taken together, the ellipsometry, thermal desorption, LSV, and faradaic efficiency data provide evidence that a major difference between $NiP_{20°C}$ and $NiP_{80°C}$ films is the presence of excess hydrogen in the electrodeposited $NiP_{20°C}$ films (Figures 3, S5). Due to the higher co-generation of $H_2(g)$ during $NiP_{20°C}$ electrodeposition, H_2 can be entrained in the electrodepositing film, creating stresses, causing hydrogen embrittlement, and/or enabling the development of defective areas. Stress corrosion cracking can occur at these defective sites upon exposure of a $NiP_{20°C}$ sample to acidic environments. Consistently, bubbles were released from the surface of the etching $NiP_{20°C}$ material, and deep cracks subsequently formed. At 80 °C, the faradaic efficiency for Ni-P deposition is higher than at 20 °C, thus less parasitic hydrogen is formed during deposition, no bubbles were visually present on the electrode surface during electrodeposition, and less hydrogen was entrained in the $NiP_{80°C}$. Although some surface-level cracking was observed in etched $NiP_{80°C}$ films, trans-film voids did not form on $NiP_{80°C}$ samples, and the $NiP_{80°C}$ samples thus do not become substantially more optically transmissive upon etching. The heated $NiP_{20°C}$ film exhibited similar optical properties to that of an as-deposited $NiP_{80°C}$ film because annealing resulted in a H_2-deficient structure similar to that obtained by depositing the film at 80 °C. In industrial plating applications, thermal treatments are well-known to drive off hydrogen and remove film weakness imparted by hydrogen embrittlement.[24-25]

Cyclic voltammograms of $n^+Si/Ti/Ni/NiP$ electrodes in 0.50 M H_2SO_4 showed that the overpotential ($\eta_{-10 \text{ mA cm}^{-2}}$) for the HER, defined herein as the excess potential beyond the thermodynamic minimum value required to produce -10 mA cm^{-2} of current density, increased monotonically from -200 mV to -230 mV, -290 mV, and -330 mV vs. RHE for the $NiP_{20°C}$, $NiP_{40°C}$, $NiP_{60°C}$, and $NiP_{80°C}$ films, respectively (Figure 4a). The catalytic activity of these electrodeposited Ni-P films is consistent with previous reports (Table S3).[15, 18] The η required for $Cu/Ti/Ni/NiP$ electrodes to produce -10 mA cm^{-2} in 0.50 M H_2SO_4 increased over time, with final measured $\eta_{-10 \text{ mA cm}^{-2}}$ of -250 mV, -300 mV, -380 mV, and -490 mV vs. RHE for the $NiP_{20°C}$, $NiP_{40°C}$, $NiP_{60°C}$, and $NiP_{80°C}$ films, respectively, after 150 min of sustained cathodic current (Figure 4b). Figure 4c shows the changes in k for as-deposited $NiP_{20°C}$ to $NiP_{80°C}$ films as the deposition temperature increased.
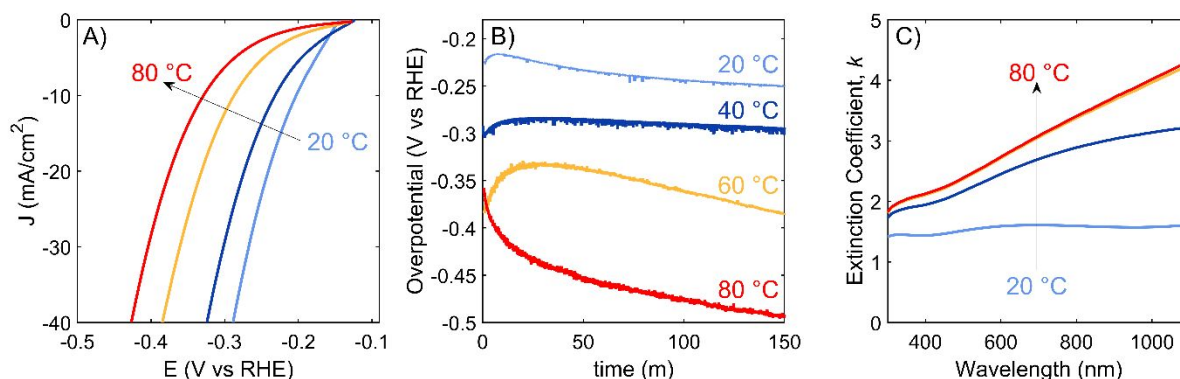
Figure 4. (a) Cyclic voltammograms of Ni-P films electrodeposited at 20 °C (light blue), 40 °C (dark blue), 60 °C (orange), and 80 °C (red) in 0.5 M H_2SO_4. (b) Overpotential measurements at -10 mA cm^{-2} for electrodeposited Ni-P films in 0.5 M H_2SO_4. (c) Extinction coefficient (k) from spectroscopic ellipsometry of electrodeposited Ni-P films on silicon substrates.

The smooth transition in catalytic and optical properties of the Ni-P films deposited between 20 °C to 80 °C indicates that the optical, corrosion-resistance, and catalytic properties of electrodeposited Ni-P films can be directly manipulated by control of the deposition bath temperature. Hydrogen dissolution, adsorption, and/or absorption lowers the overpotential for the HER for electrodeposited catalysts of Ni-S, Ni-P, Co-P, and Fe-Ni.[23, 26-27] For Ni-P, electrodeposition at room temperature leads to an increased uptake of hydrogen during deposition, reducing the HER overpotential.[23] The activity of this family of catalysts is related to their ability to adsorb hydrogen, consistent with the observed improvement in the HER activity for Ni-P films deposited at room temperature relative to films deposited at higher temperatures.

In summary, catalytically active Ni-P films were electrodeposited at a range of deposition bath temperatures. The lower faradaic efficiency for Ni-P deposition at room temperature led to a higher parasitic HER current density during Ni-P electrodeposition, resulting in visible H_2 bubbles on the working electrode surface that entrained H_2 in the depositing $NiP_{20°C}$ layer. The stresses caused by this process were released upon exposure to acidic environments, causing deep cracks to form in the $NiP_{20°C}$ films, thereby allowing light to pass through to the light-absorbing semiconductor substrate. This cracking mechanism has been observed previously in electrodeposited Co-P catalysts, indicating that the process may be generalizable to other metal-phosphide materials.[14] By increasing the temperature during electrodeposition, the parasitic HER is suppressed, which causes the optical properties of the Ni-P film to be similar to the properties

of pure metallic nickel. The transition between these two behaviors occurs gradually as the temperature is varied, facilitating control over the catalytic activity and optical transmissivity of the resulting films.

Supporting Information

Detailed experimental procedures; scanning electron micrographs, color photographs, atomic force micrographs, X-ray photoelectron spectra, energy-dispersive X-ray spectra, and UV-Vis transmission spectra of Ni-P films; anodic stripping experiments.

Conflict of Interest

NSL is a scientific founder of and consultant to a company, H2U Technologies, that is developing catalysts and electrolyzers for the production of hydrogen.

Acknowledgements

References

1.   Walter, M. G.; Warren, E. L.; McKone, J. R.; Boettcher, S. W.; Mi, Q.; Santori, E. A.; Lewis, N. S., Solar Water Splitting Cells. *Chem. Rev.* **2010,** *110* (11), 6446–6473.

2.   Sun, K.; Moreno-Hernandez, I. A.; Schmidt, W. C.; Zhou, X.; Crompton, J. C.; Liu, R.; Saadi, F. H.; Chen, Y.; Papadantonakis, K. M.; Lewis, N. S., A comparison of the chemical, optical and electrocatalytic properties of water-oxidation catalysts for use in integrated solar-fuel generators. *Energy Environ. Sci.* **2017,** *10* (4), 987-1002.

3.   Oh, S.; Oh, J., High Performance and Stability of Micropatterned Oxide-Passivated Photoanodes with Local Catalysts for Photoelectrochemical Water Splitting. *The Journal of Physical Chemistry C* **2015,** *120* (1), 133-141.

4.   Ji, L.; McDaniel, M. D.; Wang, S.; Posadas, A. B.; Li, X.; Huang, H.; Lee, J. C.; Demkov, A. A.; Bard, A. J.; Ekerdt, J. G.; Yu, E. T., A silicon-based photocathode for water reduction with an epitaxial $SrTiO_3$ protection layer and a nanostructured catalyst. *Nat Nanotechnol* **2015,** *10* (1), 84-90.

5.   Vijselaar, W.; Westerik, P.; Veerbeek, J.; Tiggelaar, R. M.; Berenschot, E.; Tas, N. R.; Gardeniers, H.; Huskens, J., Spatial decoupling of light absorption and catalytic activity of Ni–Mo-loaded high-aspect-ratio silicon microwire photocathodes. *Nature Energy* **2018,** *3* (3), 185-192.

6.   Kempler, P. A.; Gonzalez, M. A.; Papadantonakis, K. M.; Lewis, N. S., Hydrogen Evolution with Minimal Parasitic Light Absorption by Dense Co–P Catalyst Films on Structured p-Si Photocathodes. *ACS Energy Lett.* **2018,** *3* (3), 612-617.

7.   Yalamanchili, S.; Kempler, P. A.; Papadantonakis, K. M.; Atwater, H. A.; Lewis, N. S., Integration of electrocatalysts with silicon microcone arrays for minimization of optical and overpotential losses during sunlight-driven hydrogen evolution. *Sustain. Energy Fuels* **2019,** *3* (9), 2227-2236.

8.   Vijselaar, W.; Tiggelaar, R. M.; Gardeniers, H.; Huskens, J., Efficient and Stable Silicon Microwire Photocathodes with a Nickel Silicide Interlayer for Operation in Strongly Alkaline Solutions. *ACS Energy Lett.* **2018,** *3* (5), 1086-1092.

9.   Kempler, P. A.; Richter, M. H.; Cheng, W.-H.; Brunschwig, B. S.; Lewis, N. S., Si Microwire-Array Photocathodes Decorated with Cu Allow CO2 Reduction with Minimal Parasitic Absorption of Sunlight. *ACS Energy Lett.* **2020,** *5* (8), 2528-2534.

10.   Kast, M. G.; Enman, L. J.; Gurnon, N. J.; Nadarajah, A.; Boettcher, S. W., Solution-deposited $F:SnO_2/TiO_2$ as a base-stable protective layer and antireflective coating for microtextured buried-junction H_2-evolving Si photocathodes. *ACS Appl Mater Interfaces* **2014,** *6* (24), 22830-7.

11.   Heller, A.; Aspnes, D. E.; Porter, J. D.; Sheng, T. T.; Vadimsky, R. G., "Transparent" metals preparation and characterization of light-transmitting platinum films. *J. Phys. Chem.* **1985,** *89*, 4444-4452.

12.   Labrador, N. Y.; Li, X.; Liu, Y.; Tan, H.; Wang, R.; Koberstein, J. T.; Moffat, T. P.; Esposito, D. V., Enhanced Performance of Si MIS Photocathodes Containing Oxide-Coated Nanoparticle Electrocatalysts. *Nano Lett* **2016,** *16* (10), 6452-6459.

13.   Carim, A. I.; Meier, M. C.; Kennedy, K. M.; Richter, M. H.; Hamann, K. R.; Lewis, N. S., Assessing Effects of Near-Field Synergistic Light Absorption on Ordered Inorganic Phototropic Growth. *J. Am. Chem. Soc.* **2021,** *143* (10), 3693-3696.

14.   Kempler, P. A.; Fu, H. J.; Ifkovits, Z. P.; Papadantonakis, K. M.; Lewis, N. S., Spontaneous Formation of >90% Optically Transmissive, Electrochemically Active CoP Films for Photoelectrochemical Hydrogen Evolution. *J Phys Chem Lett* **2020,** *11* (1), 14-20.

15.   Callejas, J. F.; Read, C. G.; Roske, C. W.; Lewis, N. S.; Schaak, R. E., Synthesis, Characterization, and Properties of Metal Phosphide Catalysts for the Hydrogen-Evolution Reaction. *Chemistry of Materials* **2016,** *28* (17), 6017-6044.

16.   Roberts, E. J.; Read, C. G.; Lewis, N. S.; Brutchey, R. L., Phase Directing Ability of an Ionic Liquid Solvent for the Synthesis of HER-Active Ni2P Nanocrystals. *ACS Applied Energy Materials* **2018,** *1* (5), 1823-1827.

17.   Popczun, E. J.; McKone, J. R.; Read, C. G.; Biacchi, A. J.; Wiltrout, A. M.; Lewis, N. S.; Schaak, R. E., Nanostructured nickel phosphide as an electrocatalyst for the hydrogen evolution reaction. *J. Am. Chem. Soc.* **2013,** *135* (25), 9267-70.

18.   Hu, C.; Lv, C.; Liu, S.; Shi, Y.; Song, J.; Zhang, Z.; Cai, J.; Watanabe, A., Nickel Phosphide Electrocatalysts for Hydrogen Evolution Reaction. *Catalysts* **2020,** *10* (2).

19.   Morikawa, T.; Nakade, T.; Yokoi, M.; Fukumoto, Y.; Iwakura, C., Electrodeposition of Ni-P alloys from Ni-citrate bath. *Electrochim. Acta* **1997,** *42* (1), 115-118.

20.   Brennert, A.; Coucht, D. E.; Williams, E. K., Electrodeposition of Alloys of Phosphorus with Nickel or Cobalt. *Journal of Research of the National Bureau of Standards* **1950,** *44*, 109-122.

21.   Qiao, X.; Li, H.; Zhao, W.; Li, D., Effects of deposition temperature on electrodeposition of zinc–nickel alloy coatings. *Electrochim. Acta* **2013,** *89*, 771-777.

22.   Fleischmann, M.; Saraby-Reintjes, A., The simultaneous deposition of nickel and hydrogen on vitreous carbon. *Electrochim. Acta* **1984,** *29* (1), 69-75.

23.   Paseka, I.; Velicka, J., Hydrogen evolution and hydrogen sorption on amorphous smooth Me-P(x) (Me = Ni, Co, and Fe-Ni) electrodes. *Electrochim. Acta* **1997,** *42* (2), 237-242.

24.   Lee, J. A. *Hydrogen Embrittlement*; NASA: Huntsville, Alamaba, 2016.

25.   SAE, Hydrogen Embrittlement Relief (Baking) of Steel Parts: AMS2759/9E. Warrendale, PA, 2018.

26.   Paseka, I., Evolution of hydrogen and its sorption on remarkable active amorphous smooth Ni-P(x) electrodes. *Electrochim. Acta* **1995,** *40* (11), 1633-1640.

27.   Paseka, I., Sorption of hydrogen and kinetics of hydrogen evolution on amorphous $Ni-S_x$ electrodes. *Electrochim. Acta* **1993,** *38* (16), 2449-2454.